Journal of Magnetism and Magnetic Materials 523 (2021) 167562

Contents lists available at ScienceDirect

Journal of Magnetism and Magnetic Materials

journal homepage: www.elsevier.com/locate/jmmm

Antiferromagnetic resonance in $TmFeO_3$ at high temperatures

J. Zhang [a], M. Białek [b,*], A. Magrez [b], H. Yu [a], J.-Ph. Ansermet [b]

[a] Fert Beijing Institute, School of Microelectronics, Beijing Advanced Innovation Center for Big Data and Brain Computing, Beihang University, Beijing 100191, China
[b] Institute of Physics, École Polytechnique Fédérale de Lausanne (EPFL), 1015 Lausanne, Switzerland

A B S T R A C T

Temperature dependence of the antiferromagnetic resonance spectrum in a thulium orthoferrite ($TmFeO_3$) poly-crystalline sample was studied by transmission spectroscopy in the frequency range of 0.1–0.75 THz and temperature range of 300–670 K, up to its Néel temperature. We observed quasi-ferromagnetic resonance and the quasi-antiferromagnetic resonance modes. The temperature dependence of the resonance frequencies, linewidths, and amplitudes were extracted. The resonance spectrum of $TmFeO_3$ near its Néel temperature was directly observed and a drastic drop in resonance frequency for both modes was observed.

1. Introduction

Antiferromagnetic materials are under intensive research during recent years owing to their terahertz (THz) frequencies dynamics, indifference to external magnetic fields and to the abundance of materials available [1–4]. However their magnetic properties strongly depend on temperature and that might be an obstacle for their use in applications. Here, we study the temperature dependence of the antiferromagnetic resonance (AFMR) in thulium orthoferrite ($TmFeO_3$), a room-temperature antiferromagnet, studied since the 1960s [1,5–11] for its interesting optical [12–15] and antiferromagnetic [16–24] properties, such as the spin reorientation transition [25–32] or at cryogenic temperatures, electric dipole transitions in the Tm subsystem at about 0.6 THz [33–35]. However, these studies are mainly at low temperatures and resonance frequencies are mostly indirectly obtained isolated data points. In this work, the temperature dependence of the antiferromagnetic resonance in $TmFeO_3$ is studied at high temperatures by a continuous-wave method.

Thulium ferrite crystallizes in orthorhombic Pbnm space group. Below the Néel temperature $T_N = 635$ K [36] Fe^{3+} ions orient in a G-type antiferromagnetic order. Superexchange Dzialoshinskii-Moriya interaction leads to canting of neighbouring antiferromagnetically oriented spins, that gives a net magnetisation **m**, making this material a weak ferromagnet. Above the spin-reorientation transition at about 90 K, the symmetry of the magnetic system is that of the Γ_4 phase, with antiferromagnetic vector **G** laying along *a* axis and **m** in *c* axis [1]. Due to the spin canting, the antiferromagnetic resonance has two modes, the quasi-antiferromagnetic resonance (qAFMR) mode at higher frequency, exited when a dynamical magnetic field **h** is parallel to the magnetization ($\mathbf{h}\|\mathbf{m}$), and the quasi-ferromagnetic resonance (qFMR) mode at lower frequency, excited when $\mathbf{h}\perp\mathbf{m}$.

2. Samples and experiment

Thanks to the development of frequency extenders to vector network analyzers (VNA), continuous-wave spectroscopic measurements up to 1.5 THz can be rapidly conducted with a high frequency resolution and with a very high dynamic range [37–40]. We investigated a pelletized powder sample of $TmFeO_3$ of $d = 1.28$ mm in thickness and 15 mm in lateral diameter. $TmFeO_3$ was produced from Tm_2O_3 and Fe_2O_3. The two powders were mixed in stoichiometric amount and pressed into a pellet. The pellet was annealed for a week in air at 1200 °C with intermediate grinding. X-ray diffraction experiment confirmed that our sample is thulium ferrite [41] with a precision on the chemical composition of about 1%. During the THz transmission experiment, the pellet was placed between two oversized cylindrical metallic waveguides of 11 mm in inner diameter. These were fixed inside a cylindrical ceramic furnace under PID-controlled temperature measured with a K-type thermocouple positioned close to the sample. The terahertz radiation generated by the source frequency-extender passed the sample and was detected by the detector frequency-extender, as illustrated in Fig. 2. After stabilizing temperature T of the sample, we obtained a transmission spectrum as a function of radiation frequency f. Recorded spectra were obtained by averaging 20 single spectra measured with an intermediate frequency bandwidth of 100 Hz. The procedure was repeated separately in frequency bands of 100–170 GHz, 200–350 GHz, 330–500 GHz, 480–750 GHz using different sets of frequency-extenders. We recorded the relative power of transmitted radiation in units of *dB*

* Corresponding author.
E-mail address: marcin.bialek@epfl.ch (M. Białek).

https://doi.org/10.1016/j.jmmm.2020.167562
Received 11 September 2020; Received in revised form 22 October 2020; Accepted 6 November 2020
Available online 28 November 2020

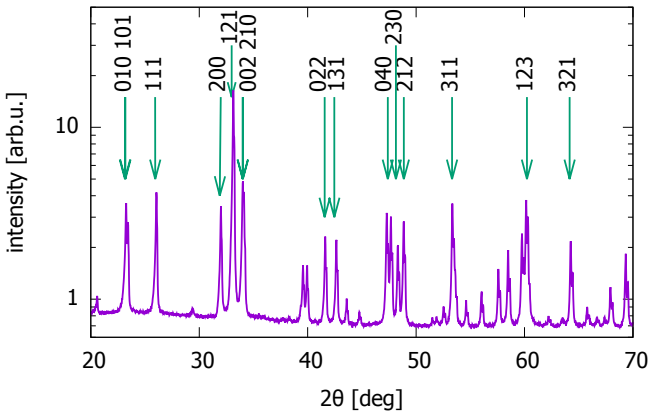

Fig. 1. Experimental X-ray diffraction pattern (purple line). All observed peaks belong to $TmFeO_3$, stronger theoretical $TmFeO_3$ peaks are marked with green arrows. (For interpretation of the references to color in this figure legend, the reader is referred to the web version of this article.)

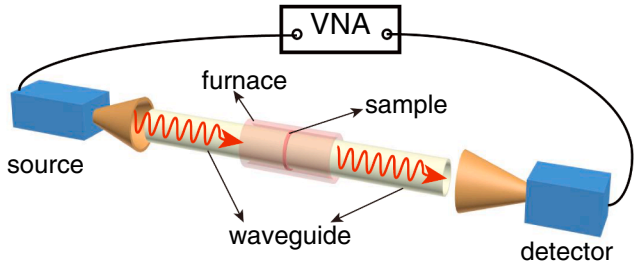

Fig. 2. Schematic of the experimental setup.

and the phase of transmitted electric field in units of degrees. Thus, a complex transmission data matrix $S_{21}(f,T)$ was obtained.

3. Results and analysis

In each frequency band, we changed temperature starting from the highest temperature with a step of $\Delta T = -1$ K. The data displayed in Fig. 3(a,c) are temperature derivative spectra obtained by subtracting amplitude of two neighbouring spectra

$$\frac{d|S_{21}(f,T)|}{dT} = \frac{|S_{21}(f,T+\Delta T)| - |S_{21}(f,T)|}{\Delta T}, \tag{1}$$

and for the phase

$$\frac{d(\arg S_{21}(f,T))}{dT} = \frac{arg(S_{21}(f,T+\Delta T)) - arg(S_{21}(f,T)))}{\Delta T}. \tag{2}$$

Our result shows two strong resonances softening with rising temperature when approaching T_N. The signal from the lower-frequency mode (qFMR) disappears near room temperature. Actually, the qFMR resonance mode is still present, it does not show up in temperature-differential spectra because it is almost temperature-independent in the temperature range of 300–400 K. Periodical horizontal modes are Fabry-Pérot type cavity modes of the sample related to its thickness. Features of alternating amplitude at 0.56 THz are related to changes in resonant absorption by water vapor. In Fig. 3(b,d), we show a fit of temperature-differential spectra using an electrodynamics-based model [40]:

$$\frac{d|S_{21}(f,T)|}{dT} = \frac{20}{\Delta T} log_{10} \frac{|t(f,T+\Delta T)|}{|t(f,T)|}, \tag{3}$$

where t is transmittance of a plane electromagnetic wave normal-incident on a parallel-plane slab of infinite lateral dimensions and thickness d:

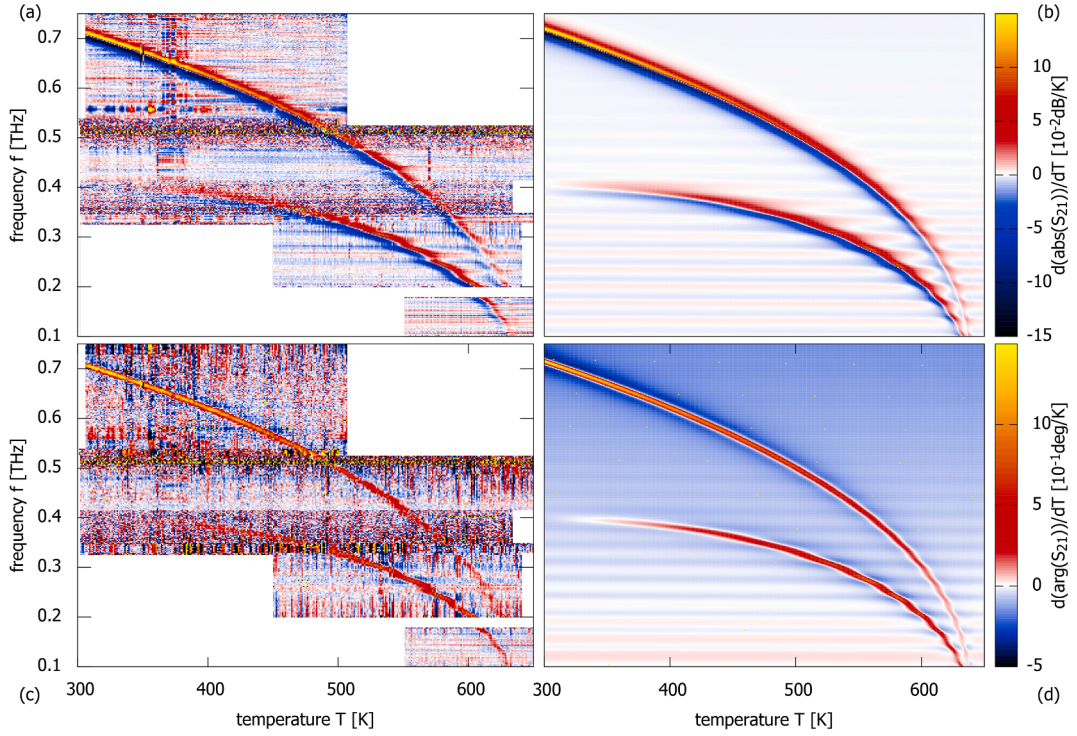

Fig. 3. The experimental temperature-differential transmission spectra S_{21} in magnitude (a) and phase (c). Global fit in magnitude (b) and phase (d), calculated using Eq. (3)–(8) with parameters from Table 1.

$$t(f,T) = \frac{(1-r^2)e^{ikd}}{1-r^2e^{2ikd}}, \tag{4}$$

where $r = (\sqrt{\epsilon}-\sqrt{\mu})/(\sqrt{\epsilon}+\sqrt{\mu})$ and $k = 2\pi f\sqrt{\epsilon\mu}/c$, with an isotropic slab material described by permeability $\mu(f,T)$ and permittivity $\epsilon(f,T)$. The assumptions that were used to obtain the fit in Fig. 3(b,d) are explained in following paragraphs.

Because the sample is composed of randomly oriented crystal grains, both the modes can be excited at any direction of incident wave polarization. Also, because the crystal grains fill only $p = 0.64$ of the sample volume [42], we assume effective dielectric function [43,44] $\sqrt{\epsilon} = p\sqrt{\epsilon_c}+(1-p)$ and similarly $\sqrt{\mu} = p\sqrt{\mu_c}+(1-p)$, where ϵ_c and μ_c are mean crystalline permittivity and permeability, respectively.

In order to carry out a quantitative analysis of the observed magnetic resonances, we fitted the amplitude of temperature-differential spectra with Eq. (3), assuming heuristic material properties of permittivity and permeability. In our model, ϵ is described by a single oscillator, that is a valid approximation because our frequency range is far from optical phonons [45]. We assumed that the oscillator strength in ϵ is weakly dependent on temperature:

$$\epsilon_c(f,T) = (a+b(T-T_0))\frac{f_p^2}{f_p^2-f^2-ifg_p}, \tag{5}$$

where $T_0 = 400\,\mathrm{K}$, $a = 22.37, b = 2.70{\cdot}10^{-3}\,\mathrm{K}^{-1}$, $f_p = 3.183\,\mathrm{THz}$ and $g_p = 1.456\,\mathrm{THz}$. Values of permittivity obtained using Eq. (5) outside our experimental spectral and temperature ranges are extrapolations. Absorption grows strongly with frequency, resulting with a very weak interference pattern at higher frequencies. We assumed that

$$\mu_c(f,T) = 1+\sum_{j=1}^{2}\frac{\Delta\mu_j f_j^2}{f_j^2-f^2-ifg_j}, \tag{6}$$

where $j = 1$ stands for the qFMR and $j = 2$ stands for the qAFMR, $\Delta\mu_j$ is a response to a static magnetic field, f_j are modes frequencies and g_j modes widths.

In order to better describe the temperature dependence of the antiferromagnetic resonance, we first fitted the resonance frequency, amplitude, and linewidth of the modes in temperature intervals, 10 K in width. Within each such interval, we put amplitudes and widths constant with temperature and we assumed that frequencies of the resonances are described by a second order polynomial. Results of these temperature interval fittings are shown as points in Fig. 4(a,b). We show in Fig. 4(a) middle frequencies of modes obtained in each temperature interval. Theses results allow us to assume some simple functional dependences that are valid in the entire experimental temperature range. First, we assumed that the amplitudes of the resonances $\Delta\mu_j$ are constant with temperature. Second, we assumed a modified power law [46]:

$$f_j(T) = f_j^{(0)}\sqrt{1+\kappa_j T}\left(1-T/T_N^{(j)}\right)^{\beta_j}, \tag{7}$$

where $f_j^{(0)}$ has frequency units, $T_N^{(j)}$ is a parameter close to the Néel temperature and a power factor expected to be $\beta_j \approx 1/3$. We modified the classical power law by putting $\kappa_j \neq 0$. Finally, we assumed that temperature dependence of widths of modes is described by a sum of a linear and an exponential functions

$$g_j(T) = g_{400}^{(j)} + g_l^{(j)}(T-400) + g_e^{(j)}e^{g_s^{(j)}(T-T_N^{(j)})}, \tag{8}$$

where the first therm is dominant at lower temperatures and the latter dominates close to T_N. We comment on these assumptions in the next section.

4. Discussion

The global fitting result, using the above assumptions, are displayed in Fig. 3(b) and (d). The fit parameter values are given in Table 1. Functions used to describe modes frequencies, amplitudes and widths are drawn as solid lines in Fig. 4. Parameters in Table 1 give good estimations of properties of magnetic resonance only in the experimental ranges of 300–650 K and 0.1–0.7 THz.

As displayed in Fig. 4(a), the frequencies of both modes decrease with temperature in the temperature range from 300 K to T_N. The frequency of the qFMR mode is almost constant near room temperature, which can be clearly observed in the differential spectra as displayed in Fig. 3, in which the resonance can be barely seen. Indeed, fit parameters of κ_1 and κ_2 show that the modification of power law behaviour is only

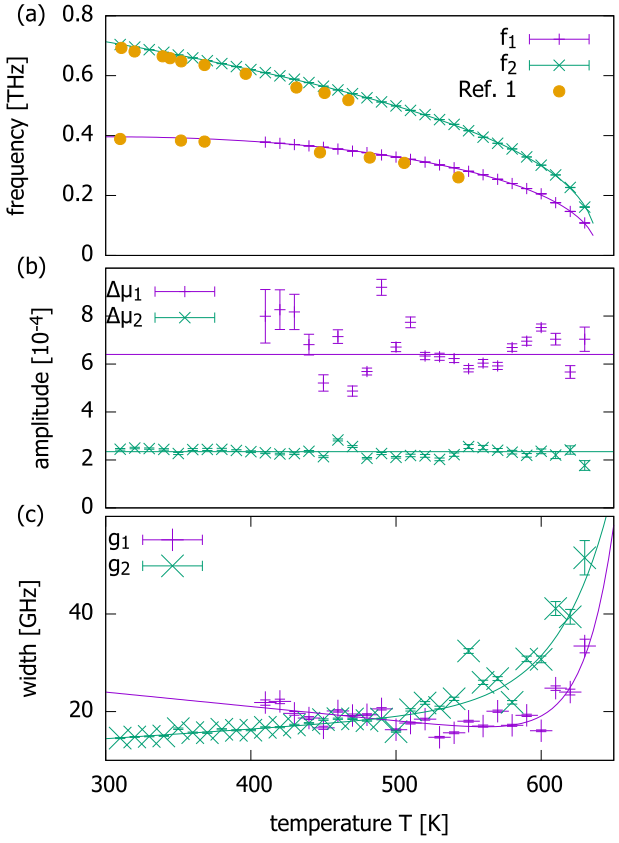

Fig. 4. The temperature dependence of the resonance in frequency (a), amplitude (b) and width (c). Points come from 10 K intervals fits. The solid lines are calculated using Eq. (7)–(8) with parameters from Table 1. The qFMR is marked purple and the qAFMR is marked green. In (a), orange points come from Ref. [1]. (For interpretation of the references to color in this figure legend, the reader is referred to the web version of this article.)

Table 1
Obtained global fit parameters.

	qFMR ($j=1$)	qAFMR ($j=2$)	unit
$\Delta\mu_j$	6.40 ± 0.16	2.34 ± 0.03	10^{-4}
$f_0^{(j)}$	232 ± 59	921 ± 5	GHz
κ_j	14 ± 9	-0.02 ± 0.05	$10^{-3}\,K^{-1}$
β_j	0.449 ± 0.011	0.399 ± 0.005	
$T_N^{(j)}$	638.9 ± 0.7	638.8 ± 0.4	K
$g_{400}^{(j)}$	21.0 ± 1.0	16.4 ± 0.3	GHz
$g_l^{(j)}$	-2.9 ± 1.1	1.9 ± 0.4	10^{-2} GHz/K
$g_e^{(j)}$	26 ± 4	33 ± 14	GHz
$g_s^{(j)}$	4.7 ± 1.3	2.8 ± 1.0	$10^{-2}\,K^{-1}$

necessary in the case of the qFMR. This is related to a temperature dependence of the magnetic anisotropy field in $TmFeO_3$ that governs the frequency of this mode. This antiferromagnet undergoes spin-reorientation transition at about 90 K, where the qFMR frequency drops nearly to zero. The actual values of β_j (Table 1) depart from the expected critical exponent of 1/3, most likely because the fits are obtained for a relatively large temperature range below T_N. Fit values of $T_N \approx 639$ K for both modes agree with each other within estimated uncertainties. The obtained value is slightly higher than in the literature ($T_N = 635$ K) [36]. This discrepancy might come from a precision of the temperature measurement in our system. As seen in Fig. 4(a), our points are at higher frequencies and higher temperatures than those of Ref. [1]. It is doubtful that this could be a result of an error in frequency measurement, since both experiments used monochromatic radiation sources of very precise frequency. An error in temperature measurement would have to be as large as about 20 K at around $T = 500$ K, that would lead to a giant discrepancy in the estimated T_N. Thus, the difference between our results and those of Ref. [1] must come from an actual difference between measured samples.

From Fig. 4(c), we see that the width of the qFMR mode (purple) experiences a slight linear decrease with temperature, while the width for the qAFMR mode (green) first experiences a linear increase. Our results are 2–3 times larger than values reported in the literature for a single crystal sample [1], that is possibly because of the poly-crystalline nature of our sample. Exponential growth of the linewidth close to the T_N is probably due to sample temperature inhomogenity or inhomogenity of T_N in the sample. We can estimate the distribution of temperatures that could cause such a broadening by solving $f_j(T) \pm \frac{1}{2}g_e^{(j)} e^{g_s^{(j)}(T-T_N^{(j)})} = f_j^{(0)}\sqrt{1+\kappa_j T}(1-T/T_{N\pm})^{\beta_j}$, thus calculating that the maximum of $T_{N+} - T_{N-}$ is about 4 K.

From Fig. 4(b), the amplitudes of both modes are constant. The amplitude of the qFMR is about twice of that of the qAFMR. This is expected, since, in our poly-crystalline sample, scalar μ_c is an average of the permeability tensor, where the qFMR has almost equal amplitudes in μ_{xx} and μ_{yy}, while the qAFMR is present only in μ_{zz}. Off-diagonal components of the permeability tensor are antisymmetric and they cancel each other in the average. Obtained amplitudes are close to those in Ref. [1], taking into account the poly-crystalline nature of our sample, in so that we observe about 1/3 of the qAFMR amplitude ($9.0 \cdot 10^{-4}$) and 2/3 of the qFMR amplitude ($8.5 \cdot 10^{-4}$).

In Fig. 5, we show measured spectra at three different temperatures, $T = 377$ K, $T = 558$ K, $T = 573$ K, as example of our analysis. We can clearly see at different temperatures, resonance frequencies and lineshapes experience changes. We observed also effects of interaction of magnetic resonance with electromagnetic standing waves in the sample slab [14,40], that are readily taken into account by electrodynamics calculations. Light-matter interaction in our case is in a weak regime, because of low quality factors of cavity modes in the sample-slab. Nevertheless, the electromagnetic cavity modes have a dramatic and nontrivial effect on observed lineshapes, as shown in Fig. 5b and c.

In Fig. 6 we show magnetic anisotropy factors $K = \mu_0 H_A M_0$, where H_A is anisotropy field and M_0 is saturation magnetisation of a sublattice. Taking that the static magnetic susceptibility $\chi_\perp = M_0/2H_E$, where H_E is exchange field, and that $\chi_\perp = 3\Delta\mu_2/\rho$, where $\rho = 8 \cdot 10^3\ \mathrm{kg/m^3}$ is $TmFeO_3$ density and the factor 3 comes from the fact the we measured about 1/3 of the qAFMR amplitude in our poly-crystalline sample. Then, solving the simplified Kittel's equation

$$2\pi f_j = \gamma\mu_0\sqrt{2H_E H_A} = \gamma\sqrt{\frac{K_j\mu_0}{\chi_\perp}}, \tag{9}$$

we find anisotropy energy density for each mode. The magnetic phase of $TmFeO_3$ is Γ_4, thus, for the qFMR mode K_1 is an anisotropy factor in the *ac* plane and for the case of the qAFMR mode the calculated K_2 anisotropy factor is for the *ab* plane [1]. We see that K_2 has almost a linear

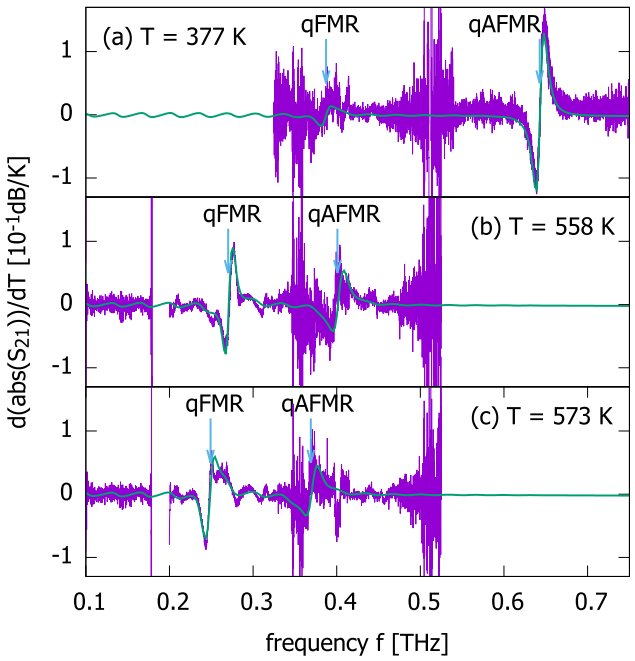

Fig. 5. Experimental spectra and fitting results at temperatures of (a) $T = 377$ K, (b) $T = 558$ K, (c) $T = 573$ K. Purple lines are experimental results while blue lines are fits. (For interpretation of the references to color in this figure legend, the reader is referred to the web version of this article.)

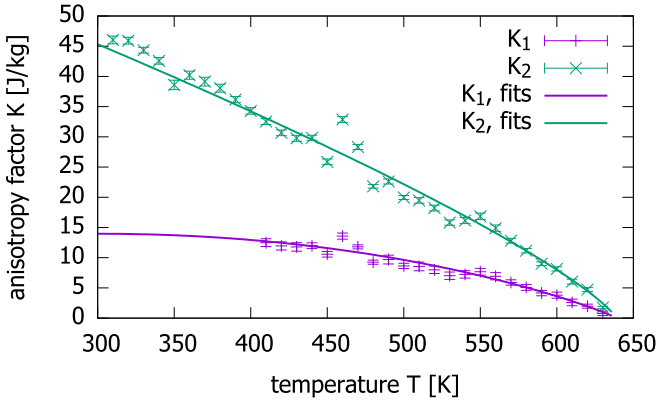

Fig. 6. Magnetic anisotropy factors K. Points where obtained using points from Fig. 4(a,b) and lines where obtained from fits presented in Fig. 4(a,b) using Eqs. (9) and (7) with parameters from Table 1.

dependence on temperature, whereas K_1 has a more complex behaviour due to the spin-reorientation transition at about 90 K. These values agree in order of magnitude with the values from Ref. [1]. Jumps of K_1 and K_2 at $T = 460$ K are artifacts caused by the qAFMR passing through the water vapor transmission line at 0.56 THz that was changing its amplitude during the measurement.

In Fig. 7, we show experimental data in an oversaturated scale that shows a very narrow feature, the frequency of which is growing with temperature from 0.2 THz at about 320 K to about 0.48 THz at 650 K. We identified this feature as the qAFMR of hematite (α-Fe_2O_3) [47]. From its amplitude (≈ 0.04 dB/K), compared to the amplitude measured in a 0.5-mm-thick single crystal hematite (≈ 30 dB/K), we can estimate that the amount of hematite impurity in our sample was about 0.2%. That is lower than the accuracy of the X-ray diffraction experiment (Fig. 1).

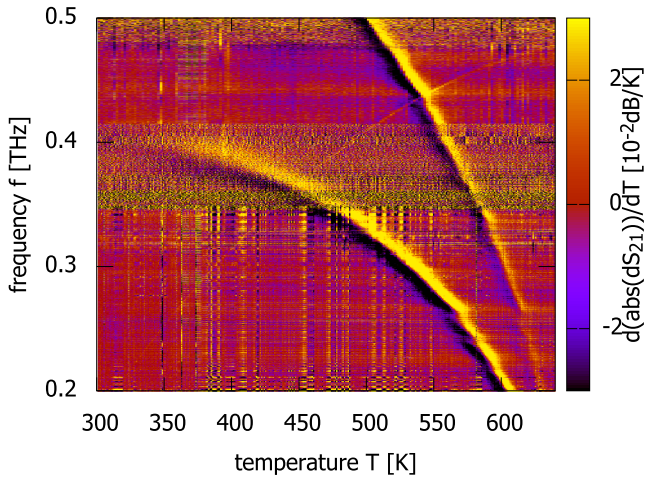

Fig. 7. Experimental spectra in an oversaturated scale that show the antiferromagnetic resonance of the hematite impurity.

5. Summary

In summary, we measured the temperature dependence of the antiferromagnetic resonance in $TmFeO_3$ poly-crystalline sample at temperatures up to 650 K, that is over its Néel temperature (T_N). Two antiferromagnetic resonance modes, the quasi-ferromagnetic and the quasi-antiferromagnetic were observed. When temperature is approaching the T_N, both resonance modes experience sharp drop in frequency. The resonance frequency, resonance width and amplitudes were extracted and fitted with an electrodynamic model. The qFMR mode resonance is nearly temperature-independent near room temperature, which may be an advantage for its use in information processing. The amplitudes of both resonance modes stay constant. The widths of both modes change linearly with temperature, at temperatures far below T_N, and both increase sharply near T_N, possibly because of inhomogeneous broadening. Using our fits we have obtained the estimation of magnetic anisotropy factors in $TmFeO_3$. Our quantitative analysis shows that light-matter coupling plays crucial role in observed lineshape. We show that our technique can detect contamination with hematite that are smaller than those detected by X-ray spectroscopy.

The data that support the findings of this study are available from the corresponding author upon reasonable request. Support by the Sino-Swiss Science and Technology Cooperation (SSSTC) Grant No. EG-CN_02_032019 is gratefully acknowledged. The VNA and frequency extenders were funded by EPFL and the SNF R'Equip under Grant No. 206021_144983.

CRediT authorship contribution statement

J. Zhang: Data curation, Investigation, Visualization, Writing - original draft. **M. Białek:** Conceptualization, Formal analysis, Investigation, Methodology, Software, Supervision, Visualization, Writing - original draft, Writing - review & editing. **A. Magrez:** Resources, Validation. **H. Yu:** Funding acquisition, Supervision, Validation, Writing - review & editing. **J.-Ph. Ansermet:** Funding acquisition, Project Administration, Supervision, Validation, Writing - review & editing.

Declaration of Competing Interest

The authors declare that they have no known competing financial interests or personal relationships that could have appeared to influence the work reported in this paper.

References

[1] A.M. Balbashov, G.V. Kozlov, A.A. Mukhin, and A.S. Prokhorov. Submillimeter spectroscopy of antiferromagnetic dielectrics: rare-earth orthoferrites, 1995, pp. 56–98.
[2] A. Kirilyuk, A.V. Kimel, T. Rasing, Ultrafast optical manipulation of magnetic order, Reviews of Modern Physics 82 (2010) 2731–2784.
[3] T. Jungwirth, X. Marti, P. Wadley, J. Wunderlich, Antiferromagnetic spintronics, Nature Nanotechnology 11 (3) (2016) 231–241.
[4] Sergio M. Rezende, Antonio Azevedo, Roberto L. Rodríguez-Suárez, Introduction to antiferromagnetic magnons, Journal of Applied Physics 126(15) (2019) 151101.
[5] A.M. Balbashov, G.V. Kozlov, S.P. Lebedev, A.M. Prokhorov, A.S. Prokhorov, Antiferromagnetic resonance in TmFeO3, Pis'ma v Zhurnal Ehksperimental'noj i Teoreticheskoj Fiziki 39 (10) (1984) 461–463.
[6] A.V. Kimel, C.D. Stanciu, P.A. Usachev, R.V. Pisarev, V.N. Gridnev, A. Kirilyuk, Th. Rasing, Optical excitation of antiferromagnetic resonance in$TmFeO_3$, Physical Review B 74 (2006), 060403 .
[7] G.V. Kozlov, S.P. Lebedev, A.A. Mukhin, A.S. Prokhorov, I.V. Fedorov, A. M. Balbashov, I.Y. Parsegov, Submillimeter backward-wave oscillator spectroscopy of the rare-earth orthoferrites, IEEE Transactions on Magnetics 29 (6) (1993) 3443–3445.
[8] S. Baierl, M. Hohenleutner, T. Kampfrath, A.K. Zvezdin, A.V. Kimel, R. Huber, R. V. Mikhaylovskiy, Nonlinear spin control by terahertz-driven anisotropy fields, Nature Photonics 10 (11) (2016) 715–718.
[9] S.A. Skorobogatov, S.E. Nikitin, K.A. Shaykhutdinov, A.D. Balaev, K.Yu. Terentjev, G. Ehlers, G. Sala, E.V. Pomjakushina, K. Conder, A. Podlesnyak, Low-temperature spin dynamics in the TmFeO3 orthoferrite with a non-Kramers ion, Physical Review B 101 (1) (2020), 014432 .
[10] S. Venugopalan, Mitra Dutta, A.K. Ramdas, J.P. Remeika, Magnetic and vibrational excitations in rare-earth orthoferrites: A Raman scattering study, Physical Review B 31(3) (1985) 1490–1497.
[11] R.V. Mikhaylovskiy, E. Hendry, V.V. Kruglyak, R.V. Pisarev, Th. Rasing, A. V. Kimel, Terahertz emission spectroscopy of laser-induced spin dynamics in $TmFeO_3$ and $ErFeO_3$ orthoferrites, Physical Review B 90 (2014), 184405 .
[12] P.A. Usachev, R.V. Pisarev, A.M. Balbashov, A.V. Kimel, A. Kirilyuk, Th. Rasing, Optical properties of thulium orthoferrite TmFeO3, Physics of the Solid State 47 (2005) 2292–2298.
[13] Z. Wang, Y. Lan, Z. Zeng, X. Chen, Q. Chen, Magnetic structures and optical properties of rare-earth orthoferrites RFeO3 (R = Ho, Er, Tm and Lu), Solid State Communications 288 (2019) 10–17.
[14] K. Grishunin, T. Huisman, G.Q. Li, E. Mishina, T. Rasing, A.V. Kimel, K.L. Zhang, Z. M. Jin, S.X. Cao, W. Ren, G.H. Ma, Rostislav V. Mikhaylovskiy, Terahertz Magnon-Polaritons in $TmFeO_3$, ACS Photonics 5 (4) (2018) 1375–1380.
[15] R.V. Mikhaylovskiy, E. Hendry, A. Secchi, J.H. Mentink, M. Eckstein, A. Wu, R. V. Pisarev, V.V. Kruglyak, M.I. Katsnelson, Th. Rasing, A.V. Kimel, Ultrafast optical modification of exchange interactions in iron oxides, Nature Communications 6 (1) (2015) 8190.
[16] R. Szymczak, A.M. Balbashov, The temperature dependence of domain wall energy in $TmFeO_3$, Physica B+C 125 (1) (1984) 40–44.
[17] A. Bombik, B. Leśniewska, A.W. Pacyna, Magnetic susceptibility of powder and single-crystal TmFeO3 orthoferrite, Journal of Magnetism and Magnetic Materials 214 (3) (2000) 243–250.
[18] J.A. Cape, A.P. Malozemoff, The low temperature magnetization of TmFeO3, Solid State Communications 8 (24) (1970) 2067–2070.
[19] F. Rossol, Temperature dependence of rare-earth orthoferrite properties relevant to propagating domain device applications, IEEE Transactions on Magnetics 5 (3) (1969) 562–565.
[20] G. Gorodetsky, S. Shaft, B.M. Wanklyn, Magnetoelastic properties of $TmFeO_3$ at the spin reorientation region, Physical Review B 14 (1976) 2051–2056.
[21] J. Guo, L. Cheng, Z. Ren, W. Zhang, X. Lin, Z. Jin, S. Cao, Z. Sheng, G. Ma, Magnetic field tuning of spin resonance in TmFeO3 single crystal probed with THz transient, Journal of Physics Condensed Matter 32 (18) (2020), 185401 .
[22] S.S. Karneeva, V.P. Kalantarian, A.P. Guess, V.V. Fedotova, R. Shimchak, M.A. Shamsutdinov, Magnetic properties of TmFeO $_3$ and $TmGa_{0.13}Fe_{0.87}O_3$ orthoferrites, Journal of Magnetism and Magnetic Materials 110(3) (1992) 327–330.
[23] K.A. Krezhov, P.S. Jajdzhiev, A.M. Kadomtseva, I.B. Krinettskii, M.M. Lukina, Magnetic structure and spin reorientation transitions in a system of manganese-substituted thulium orthoferrites, Journal of Physics C Solid State Physics 15 (31) (1982) 6437–6447.
[24] L.T. Tsymbal, Ya.B. Bazaliĭ, G.N. Kakazeĭ, Yu.I. Nepochatykh, P.E. Wigen, Natural behavior of the magnetization under spontaneous reorientation: $TmFeO_3$, $ErFeO_3$, Low Temperature Physics 31 (3) (2005) 277–282.
[25] G. Gorodetsky, S. Shaft, J.P. Remeika, Propagation of surface magnetoelastic waves in TmFeO3 at the spin reorientation, Journal of Applied Physics 52 (12) (1981) 7353–7359.
[26] A.V. Kimel, A. Kirilyuk, A. Tsvetkov, R.V. Pisarev, Th. Rasing, Laser-induced ultrafast spin reorientation in the antiferromagnet TmFeO3, Nature 429 (6994) (2004) 850–853.
[27] R. Muralidharan, T.H. Jang, C.H. Yang, Y.H. Jeong, T.Y. Koo, Magnetic control of spin reorientation and magnetodielectric effect below the spin compensation temperature in TmFeO3, Applied Physics Letters 90 (1) (2007), 012506 .
[28] K. Zhang, K. Xu, X. Liu, Z. Zhang, Z. Jin, X. Lin, B. Li, S. Cao, G. Ma, Resolving the spin reorientation and crystal-field transitions in TmFeO3 with terahertz transient, Scientific Reports 6 (2016) 23648.

[29] X. Zeng, X. Fu, X. Xi, D. Wang, J. Zhou, B. Li, Thermodynamics of spin reorientations in TmFeO3 ceramics observed with terahertz time domain spectroscopy, Materials Letters 164(C) (2016) 64–67.
[30] U. Staub, L. Rettig, E.M. Bothschafter, Y.W. Windsor, M. Ramakrishnan, S.R. V. Avula, J. Dreiser, C. Piamonteze, V. Scagnoli, S. Mukherjee, C. Niedermayer, M. Medarde, E. Pomjakushina, Interplay of Fe and Tm moments through the spin-reorientation transition in $TmFeO_3$, Physical Review B 96 (2017), 174408 .
[31] S. Schlauderer, C. Lange, S. Baierl, T. Ebnet, C.P. Schmid, D.C. Valovcin, A. K. Zvezdin, A.V. Kimel, R.V. Mikhaylovskiy, R. Huber, Temporal and spectral fingerprints of ultrafast all-coherent spin switching, Nature 569 (7756) (2019) 383–387.
[32] K. Saito, A. Sato, A. Bhattacharjee, M. Sorai, High-precision detection of the heat-capacity anomaly due to spin reorientation in TmFeO3 and HoFeO3, Solid State Communications 120 (4) (2001) 129–132.
[33] A.M. Balbashov, A.A. Volkov, G.V. Kozlov, S.P. Lebedev, A.A. Mukhin, A. Yu. Pronin, A.S. Prokhorov, A.M. Prokhorov, Observation in TmFeO3 of direct electronic transitions inside the principal multiplet of a rare-earth ion, Soviet Journal of Experimental and Theoretical Physics Letters 42 (1985) 564.
[34] G.V. Kozlov, A.A. Mukhin, A.Yu. Pronin, A.S. Prokhorov, V. Železny, J. Petzelt, Observation of magnetic dipole and electric dipole electron transitions in the ground multiplet of the rare-earth ion in TmFeO3, Soviet Journal of Experimental and Theoretical Physics Letters 52 (1990) 264.
[35] A.A. Mukhin, A.Yu. Pronin, A.S. Prokhorov, G.V. Kozlov, V. Zelezny, J. Petzelt, Submillimeter and far IR spectroscopy of magneto- and electrodipolar rare-earth modes in the orthoferrite TmFeO 3, Physics Letters A 153 (8–9) (1991) 499–504.
[36] A. Bombik, B. Lesniewska, J. Mayer, A.W. Pacyna, Crystal structure of solid solutions $REFe_{1-x}(AlorGa)_xO3$ (RE=Tb, Er, Tm) and the correlation between superexchange interaction Fe+3-O-2-Fe+3 linkage angles and Néel temperature, Journal of Magnetism and Magnetic Materials 257 (2) (2003) 206–219.
[37] C. Caspers, V.P. Gandhi, A. Magrez, E. de Rijk, J.-P. Ansermet, Sub-terahertz spectroscopy of magnetic resonance in BiFeO3 using a vector network analyzer, Applied Physics Letters 108 (24) (2016), 241109 .
[38] M. Białek, A. Magrez, A. Murk, J.-Ph. Ansermet, Spin-wave resonances in bismuth orthoferrite at high temperatures, Physical Review B 97 (2018), 054410 .
[39] M. Białek, T. Ito, H. Rønnow, J.-Ph. Ansermet, Terahertz-optical properties of a bismuth ferrite single crystal, Physical Review B 99 (2019), 064429 .
[40] M. Białek, A. Magrez, J.-Ph. Ansermet, Spin-wave coupling to electromagnetic cavity fields in dysposium ferrite, Physical Review B 101 (2020), 024405 .
[41] K. Mathew, C. Zheng, D. Winston, C. Chen, A. Dozier, J.J. Rehr, S.P. Ong, K. A. Persson, High-throughput computational x-ray absorption spectroscopy, Scientific Data 5 (1) (2018), 180151 .
[42] C. Song, P. Wang, H.A. Makse, A phase diagram for jammed matter, Nature 453 (7195) (2008) 629–632.
[43] W. Heller, The determination of refractive indices of colloidal particles by means of a new mixture rule or from measurements of light scattering, Physical Review 68 (1945) 5–10.
[44] J.R. Birchak, C.G. Gardner, J.E. Hipp, J.M. Victor, High dielectric constant microwave probes for sensing soil moisture, Proceedings of the IEEE 62(1) (1974) 93–98.
[45] H.C. Gupta, Manoj Kumar Singh, L.M. Tiwari, Lattice dynamic investigation of Raman and infrared wavenumbers at the zone center of orthorhombic RFeO3 (R = Tb, Dy, Ho, Er, Tm) perovskites, Journal of Raman Spectroscopy 33(1) (2002) 67–70.
[46] M. Eibschütz, S. Shtrikman, D. Treves, Internal field in orthoferrites and the one third power law, Solid State Communications 4 (3) (1966) 141–145.
[47] K.S. Aleksandrov, L.N. Bezmaternykh, G.V. Kozlov, S.P. Lebedev, A.A. Mukhin, A. S. Prokhorov, Anomalies of high-frequency magnetic permeability of hematite at the Morin phase transition, Journal of Experimental and Theoretical Physics 65 (3) (1986) 591.